Engineering Structures 348 (2026) 121735

Contents lists available at ScienceDirect

Engineering Structures

journal homepage: www.elsevier.com/locate/engstruct

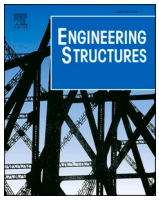

A kinematics-based model for the shear response of reinforced concrete dapped-end connections

Sameera Hippola *, Boyan I. Mihaylov

Department of ArGEnCo, University of Liège, Building B52, Quartier Polytech 1, Allée de la Découverte 9, Liège B-4000, Belgium

ARTICLE INFO

Keywords:
Dapped-end connections
Kinematics-based model
Shear behaviour

ABSTRACT

Structural assessment of reinforced concrete dapped-end connections calls for predictive models which can capture the response of the connection, including the opening of critical cracks. This paper presents such a model based on kinematics. The formulation explicitly models the critical shear crack and the concrete block above it. The concrete block is assumed rigid, except for the critical loading zone where compressive strains are localized. The displacements of the concrete block are idealized using two degrees of freedom (DOFs), which also describe the kinematics of the critical shear crack (widths and slips). The shear resisting mechanisms are calculated for a given set of DOFs using appropriate constitutive relationships. The equilibrium of the forces yields the applied load for a given displacement. The model is validated using an experimental database of 44 specimens, showing adequate predictions. The average strength experimental-to-predicted ratio is 1.03 and the coefficient of variation is 9.7 %.

1. Introduction

Reinforced concrete dapped-end connections, also termed half-joints or Gerber joints, are commonly found in precast buildings and bridges. They were most prevalent in bridge construction during the 1950s-70s as they provided statically determinate systems and allowed for rapid construction (Fig. 1a). However, these connections are inherently vulnerable due to stress concentration in the re-entrant corner, which results in wide cracks under service loads (Fig. 1b). These cracks progress due to fatigue deterioration caused by repeated loading and reinforcement corrosion caused by infiltration of water and chlorides. In addition, half-joints are also sensitive to detailing errors, especially inadequate reinforcement anchorage. Due to these reasons, many experimental and analytical studies have been conducted in the past to understand and model their behaviour.

The modelling approaches for strength of dapped-end connections available to-date include strut-and-tie models [1–4], stress-field models [5,6], empirical and semi-empirical equations [7], non-linear finite element analysis [8,9], and kinematics-based models [10,11]. Out of these approaches, strut-and-tie models are adopted in design codes [12,13] and widely used in the design of new structures. This approach has been refined by substituting the discrete struts with detailed compressive stress fields in the concrete [5,6]. Both approaches are based on the lower bound theorem of plasticity and typically do not predict deformations or crack widths for serviceability checks or assessment.

Nonlinear finite element models typically use smeared rotating crack formulations [14,15], where cracked concrete is represented as a homogenous orthotropic material. While this approach provides accurate strength predictions and global displacements, it too fails to provide a direct and accurate link between the kinematics of the critical cracks (widths and slips) and the applied load. At the same time, in terms of structural assessment of aging dapped-end connections, it is of interest to have models which link the crack widths measured on-site and the applied load on the connection.

Kinematics-based modelling [16] provides a framework to model different structural elements accommodating a direct link between kinematics of the critical crack and the applied load. These models are formulated by idealizing the deformed configuration of the connection/member using 2-3 degrees of freedom (DOFs). The idealized deformations include explicitly the widths and slips along the critical cracks. The deformations are linked to internal forces using appropriate constitutive relationships.

Rajapakse et al., 2021 [10] have proposed a kinematics-based model for flexural failures of dapped-end connections, where the failure occurs along the re-entrant corner crack due to reinforcement yielding – see Fig. 2a. This formulation explicitly models the critical flexure crack

* Corresponding author.
E-mail address: h.hippola@uliege.be (S. Hippola).

https://doi.org/10.1016/j.engstruct.2025.121735
Received 23 July 2025; Received in revised form 26 October 2025; Accepted 7 November 2025
Available online 17 November 2025

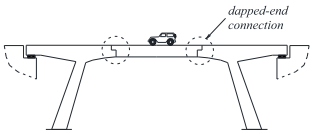

(a) Gerber-type bridge with dapped-end connections

(b) Re-entrant corner crack (photo courtesy by SPW)

Fig. 1. Dapped-end connections.

propagating from the re-entrant corner and its kinematics based on a single DOF ∅ (relative rotation of the concrete blocks on each side of the crack around the crack tip), and the compression zone depth x. This model is able to capture the resisting mechanisms contributing to the flexural strength of dapped ends such as reinforcement forces and flexural compression zone. Therefore, it is suitable for the assessment of flexure-critical dapped ends.

In addition to flexural failures, past experimental investigations have also demonstrated shear failures in the dapped-end region – see Fig. 2b. Such failures occur along a crack propagating from the inner edge of the support plate to the top end of the hanger reinforcement of the connection (critical shear crack). To address this failure mode, the current study proposes a model of the kinematics of the critical shear crack using two DOFs, which allows to compute the resisting mechanisms contributing to the shear strength of dapped-end connections. These mechanisms include reinforcement forces, critical loading zone, aggregate interlock, and dowel action. The paper presents a complete formulation of the model and its validation in terms of shear strength and widths of the critical shear crack.

2. Kinematics of flexure- and shear-critical dapped-end connections

2.1. Experimental observations

To understand the deformations of dapped-end connections, it is instructive to examine digital image correlation measurements (DIC) from a recent experimental program [17,18]. The program consisted of testing to failure of 16 full-scale specimens: 8 with orthogonal reinforcement and 8 with diagonal reinforcement. The depth of the dapped end was 500 mm and the full depth of the specimens was 1000 mm. The total area of dapped-end reinforcement (horizontal, vertical and diagonal) varied in a wide range from 697 mm^2 to 4676 mm^2. The ratio between the horizontal and vertical reinforcement was also varied in the tests – see Appendix A for all properties.

Out of the 16 specimens, the three dapped-ends with the lowest reinforcement failed in flexure, while the others exhibited shear-dominated behaviour. Fig. 3 compares the DIC-measured deformed shapes of the specimens with the minimum (OL1) and maximum (DL8) reinforcement at peak load. Specimen OL1 had an orthogonal reinforcement layout while DL8 featured a diagonal layout. The photos of

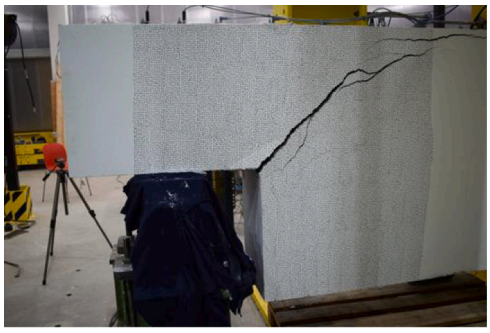

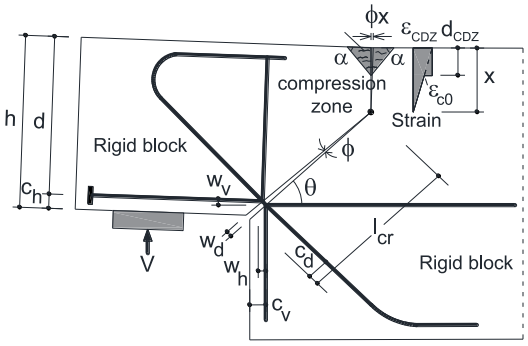

(a) Flexural failure (specimen OL1 [17]) and kinematics-based model [10]

(b) Shear failure (specimen DL8 [18])

Fig. 2. Common failure modes of dapped-end connections observed in lab tests.

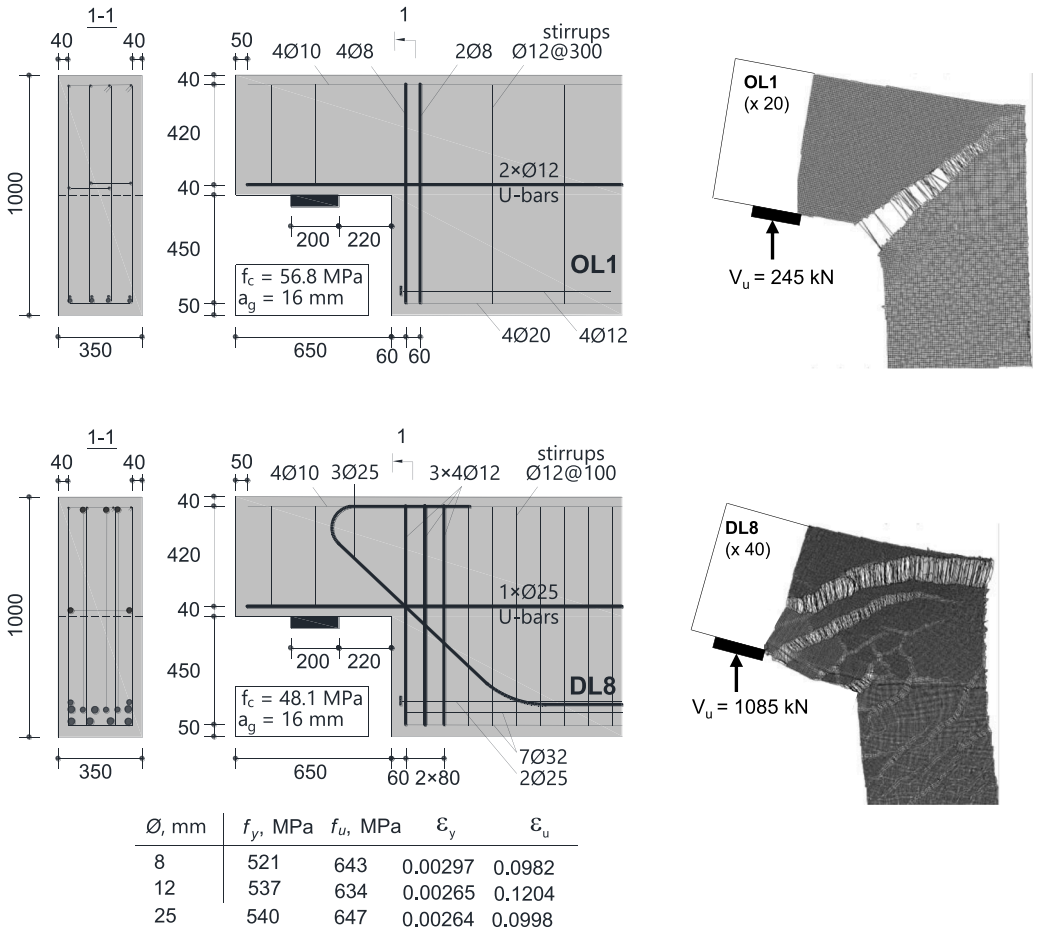

Ø, mm	f_y, MPa	f_u, MPa	ε_y	ε_u
8	521	643	0.00297	0.0982
12	537	634	0.00265	0.1204
25	540	647	0.00264	0.0998

Fig. 3. Flexure- and shear- critical dapped ends (specimens OL1 and DL8, respectively [17,18]): properties and measured deformed shapes at peak load.

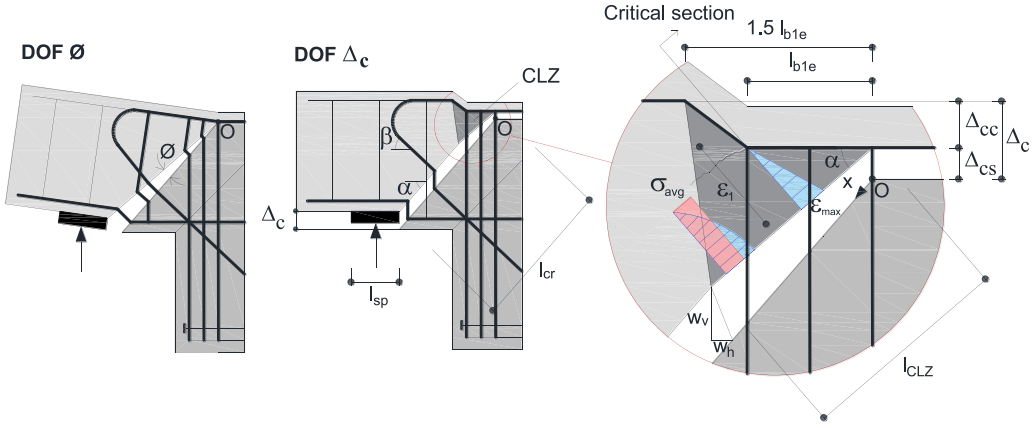

Fig. 4. Two-degrees of freedom of the kinematic model for shear-critical dapped-end connections.

the two dapped ends after failure are shown in Fig. 2.

It can be seen from Fig. 3 that the kinematics of flexure- and shear-critical dapped-end connections are distinctly different. In specimen OL1, the dapped end undergoes a rigid-body rotation around the tip of the crack through the re-entrant corner. The crack is nearly straight and opens without visible slip displacements. The crack width decreases almost linearly from the re-entrant corner to the tip of the crack.

In comparison, the deformations of the shear-critical specimen DL8 appear more complex, as it features both flexural and shear cracks. The widest crack is the critical shear crack, which is approximately straight within the dapped end and turns horizontal near the top edge of the specimen. The concrete block above the critical crack performs a rigid-body motion that is more complex compared to that in specimen OL1. Associated with this motion, the critical shear crack undergoes both opening and slip displacements. At peak load, the crack displacements are nearly vertical as consistent with the action of transverse (shear) forces. In addition, Fig. 2b shows that concrete crushing occurs above the critical crack in the top zone where the crack turns horizontal.

2.2. Kinematic model

Based on the observations from specimen DL8 and other tests, a

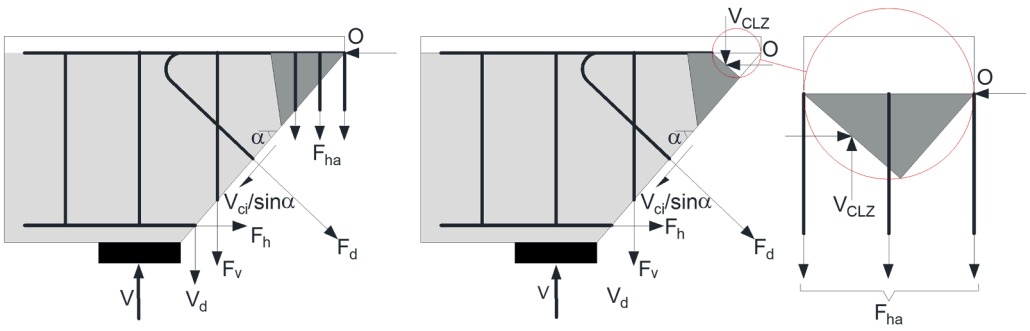

Fig. 5. Internal forces in shear-critical dapped-end connections.

kinematic model is proposed for shear-critical dapped-end connections. The model has two degrees of freedom (DOFs) as illustrated in Fig. 4. The shear crack is assumed straight and extends from the inner edge of the support to the top end of the vertical hanger reinforcement. When the connection has several hanger bars/stirrups, the crack is assumed to propagate towards the farthest bar – see point O.

The concrete block above the crack is rigid, except for the region near the top of the hanger reinforcement where the concrete crushes at shear failure. This region is termed the critical loading zone (CLZ) and was initially introduced by Mihaylov et al. [16] for modelling of deep beams. The deformations outside this region are neglected as they do not contribute to the kinematics of the critical crack, and thus do not affect significantly the shear behaviour along the crack. Rather, these deformations contribute to the global deformations of the dapped end.

The first DOF of the kinematic model is the rotation of the rigid block $\varnothing$ around point O. The second DOF is the vertical shift of the block Δ_c in the vicinity of the CLZ. As shown in Fig. 4 (right), DOF Δ_c has two components: the vertical shift due to deformations in the critical loading zone Δ_{cc}, and the vertical shift due to local elongation of the hanger bars in the critical crack Δ_{cs}. The latter component is clearly visible in Fig. 3: it is the vertical displacement in the horizontal branch of the critical crack. Therefore, DOF Δ_c is expressed as:

$$\Delta_c = \Delta_{cc} + \Delta_{cs} \tag{1}$$

The total deformations of the dapped end can be obtained by superimposing the deformation patterns associated with the two DOFs of the kinematic model.

2.3. Expressions for local deformations

The proposed kinematic model can be used to derive important deformations along the critical shear crack and within the CLZ. These deformations will be used later for evaluating the shear-resisting components across the crack. The deformations are:

- crack width w and slip s for the evaluation of aggregate interlock

$$w = \begin{cases} \varnothing x + \left(\dfrac{\Delta_{cc}}{l_{CLZ}}x + \Delta_{cs}\right)\cos\alpha & \text{if } x \le l_{CLZ} \\ \varnothing x + (\Delta_{cc} + \Delta_{cs})\cos\alpha & \text{if } x > l_{CLZ} \end{cases} \tag{2}$$

$$s = \begin{cases} \left(\dfrac{\Delta_{cc}}{l_{CLZ}}x + \Delta_{cs}\right)\sin\alpha & \text{if } x \le l_{CLZ} \\ (\Delta_{cc} + \Delta_{cs})\sin\alpha & \text{if } x > l_{CLZ} \end{cases} \tag{3}$$

-horizontal, vertical and diagonal crack displacement for the evaluation of the strains and forces in the respective reinforcement

$$w_h = \varnothing x \sin\alpha \tag{4}$$

$$w_v = \begin{cases} \varnothing x \cos\alpha + \dfrac{\Delta_{cc}}{l_{CLZ}}x + \Delta_{cs} & \text{if } x \le l_{CLZ} \\ \varnothing x \cos\alpha + \Delta_{cc} + \Delta_{cs} & \text{if } x > l_{CLZ} \end{cases} \tag{5}$$

$$w_d = \begin{cases} \varnothing x \sin(\alpha+\beta) + \left(\dfrac{\Delta_{cc}}{l_{CLZ}}x + \Delta_{cs}\right)\sin\beta & \text{if } x \le l_{CLZ} \\ \varnothing x \sin(\alpha+\beta) + (\Delta_{cc} + \Delta_{cs})\sin\beta & \text{if } x > l_{CLZ} \end{cases} \tag{6}$$

- compressive strains along the bottom edge of the CLZ [16] for the evaluation of the stresses and force in the CLZ

$$\varepsilon_{\max} = \frac{\Delta_{cc}\sin\alpha}{l_{CLZ}} \tag{7}$$

where α is the angle of the critical crack, x is a coordinate along the crack measured away from point O, an l_{CLZ} is the length of the CLZ along the critical crack:

$$l_{CLZ} = \min(3l_{b1e}\cos\alpha, l_{cr}) \tag{8}$$

Eqs. (2)-(8) are derived directly from the kinematics in Fig. 4. The geometry of the CLZ, including length l_{CLZ}, has been derived elsewhere [16]. Quantity l_{b1e} is the length of distribution of the vertical hanger reinforcement, while l_{cr} is the length of the entire critical shear crack (Fig. 4).

The next section describes how the various shear-resisting mechanisms in dapped-end connections are calculated from the deformations given by Eqs. (2)-(8).

3. Shear-resisting mechanisms of dapped-end connections

The shear-resisting mechanisms can be defined by studying the equilibrium of the concrete block above the critical shear crack – see Fig. 5.

The free-body diagram in Fig. 5 (left) shows that the shear force V applied on the dapped end is resisted by the vertical hanger reinforcement F_{ha}, stirrups F_v and diagonal reinforcement F_d in the dapped end, as well as aggregate interlock V_{ci} and dowel action of the bottom horizontal reinforcement V_d. On the other hand, if the free body in Fig. 5 (right) is considered, component F_{ha} can be replaced by the shear carried in the critical loading zone V_{CLZ}. This is because the two mechanisms act in series as depicted within the circled region in figure. Consequently, the weaker of the concrete CLZ and hanger reinforcement will limit the shear carried at the top of the critical shear crack. All shear-resisting mechanisms discussed above are individually modelled in the following subsections.

3.1. Critical loading zone and hanger reinforcement

The CLZ shown in Fig. 4 (right) idealizes the region of concrete where high compressive strains are localized. Its geometry is determined by the distribution length of hanger reinforcement l_{b1e} and the angle of the critical crack α [16]. The CLZ is "loaded" by the hanger bars and its vertical deflection is Δ_{cc}. The shear force in the CLZ V_{CLZ} is therefore linked to deformation Δ_{cc}. At the same time, the tension in the hanger bars F_{ha} depends on the vertical opening of the critical crack w_v, which in

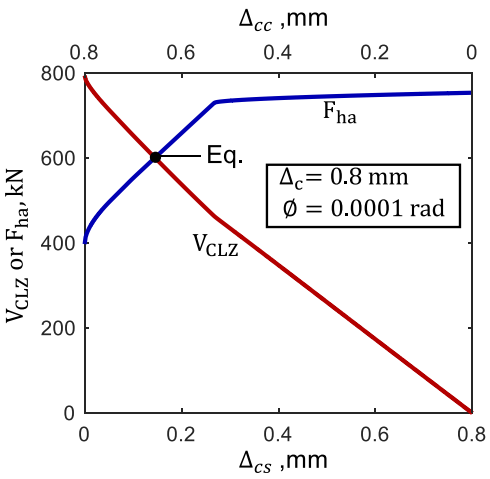

Fig. 6. Determination of state of the CLZ using the properties of specimen DL8 [18].

turn depends on deformations Δ_{cc}, Δ_{cs} and ∅ (Eq. 5). Therefore, for the modelling of the CLZ and hanger reinforcement, it is necessary to first express V_{CLZ} and F_{ha} in terms of Δ_{cc} and $w_v(\Delta_{cc}, \Delta_{cs}, \varnothing)$, respectively.

Relationship $V_{CLZ}(\Delta_{cc})$ has been derived elsewhere for deep beams [16,19]:

$$V_{CLZ}(\Delta_{cc}) = k_c \sigma_{avg} b l_{b1e} \sin^2\alpha \tag{9}$$

$$k_c = \min\left(\frac{1}{0.8 + 170\varepsilon_1}, 1\right) \tag{10}$$

$$\varepsilon_1 = \frac{0.5\sigma_{ha}}{E_s}(1 + \tan^2\alpha) \tag{11}$$

where the terms of this equation are illustrated in Fig. 4 (right). Term $\sigma_{avg}[\varepsilon_{max}(\Delta_{cc})]$ is the average stress in the critical section of the CLZ, $\varepsilon_{max}(\Delta_{cc})$ is the maximum strain in the critical section expressed with Eq. (7), b is the width of the section, $\sigma_{ha} = F_{ha}/A_{ha}$ is the stress in the hanger reinforcement, and E_s is the modulus of elasticity of the reinforcement. Stress σ_{avg} is obtained by averaging the Popovic's compression model [20] from zero strain to ε_{max}. Factor k_c accounts for the compression softening of the concrete in the CLZ inflicted by the tensile strains in the hanger reinforcement [14,21]. Strain ε_1 is the estimated principal tensile strain in the CLZ, which is perpendicular to the compressive strain ε_{max} (Fig. 4 right).

The relationship $F_{ha}[w_v(\Delta_{cc}, \Delta_{cs}, \varnothing)]$ is derived by considering the pullout displacement of the hanger reinforcement from the concrete above and below the critical crack. To calculate this displacement for a given pullout force F_{ha}, it is necessary to model the bond along the bars away from the crack [22]. Details on the modelling of the pullout behaviour are provided in Section 3.2.

With established functions $V_{CLZ}(\Delta_{cc})$ and $F_{ha}[w_v(\Delta_{cc}, \Delta_{cs}, \varnothing)]$, it becomes possible to obtain the complete state of the CLZ for a given set of DOFs Δ_c and ∅. This is achieved by imposing two conditions: equilibrium $F_{ha} = V_{CLZ}$ and compatibility $\Delta_c = \Delta_{cc} + \Delta_{cs}$ (Eq. 1). The equilibrium condition expresses the assumption that the CLZ and the hanger reinforcement work in series (Fig. 5 right). When the two conditions are solved simultaneously, quantities V_{CLZ}, F_{ha}, Δ_{cc}, and Δ_{cs} are determined.

Fig. 6 illustrates the solution of the CLZ of specimen DL8 at Δ_c = 0.8mm and ∅= 0.0001 rad. On the bottom horizontal axis is Δ_{cs} which is varied from zero to Δ_c. For each value of Δ_{cs}, Δ_{cc} is obtained from compatibility ($\Delta_{cc} = \Delta_c - \Delta_{cs}$). Therefore, for each value of Δ_{cs}, it is possible to calculate forces V_{CLZ} and F_{ha}. The solution of the CLZ is therefore obtained at the intersection point of curves V_{CLZ} and F_{ha} where the forces are in equilibrium. Force V_{CLZ} decreases with increasing Δ_{cs}, and F_{ha} increases with increasing Δ_{cs}. Note that the tension in the hangers is not zero even when Δ_{cs} is zero. This is due to the rotational DOF ∅, which does not appear in Fig. 6.

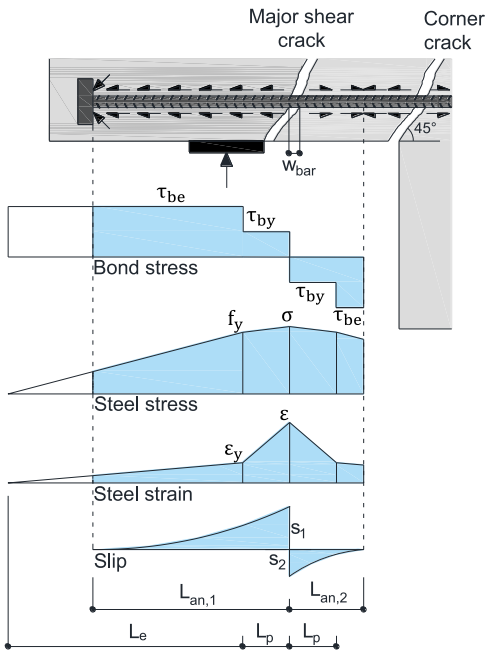

Fig. 7. Idealized bond stress, strain and slip distributions along reinforcing bars crossing cracks.

Based on the above, the operations required for the CLZ can be mathematically presented as a function f_{CLZ}:

$$V_{CLZ} = f_{CLZ}(\Delta_c, \varnothing) \tag{12}$$

3.2. Reinforcement crossing the critical shear crack

In the general case, the reinforcement crossing the critical crack is horizontal, vertical and diagonal (Fig. 5). Similarly to the CLZ, it is necessary to express the forces in the reinforcement F_h, F_v, and F_d with the DOFs of the kinematic model. The crack displacements in the direction of the reinforcement were already expressed with the two DOFs ∅ and Δ_c in Eqs. (4)-(6). Therefore, the goal of this section is to derive relationships $F_h(w_h)$, $F_v(w_v)$, and $F_d(w_d)$. The derivation will be made for a general case $F_{bar}(w_{bar})$, which will also provide the solution for relationship $F_{ha}(w_v)$ discussed earlier.

The crack displacement w_{bar} is the sum of the reinforcement pullout from either side of the crack – see Fig. 7. The pullout depends on how the force in the bar is transmitted to the concrete via bond stresses. The Tension Chord Model (TCM) proposed by Marti et al. [22] allows to evaluate the pullout (or slip displacement) s_k as a function of the reinforcement strain ε at the crack. Here the subscript k represents the side of the reinforcing bar relative to the crack (k = 1 or 2). In the TCM, the bond stress versus slip relationship is assumed rigid-plastic as shown in Fig. 7. The bond stresses prior to and after yielding of the bar τ_{be} and τ_{by}, respectively, are calculated based on the tensile strength of the concrete f_{ct}:

$$f_{ct} = 0.33\sqrt{f_c}, \text{MPa} \tag{13}$$

$$\tau_{be} = 2f_{ct} \tag{14}$$

$$\tau_{by} = f_{ct} \tag{15}$$

Based on equilibrium and a bi-linear stress-strain relationship of the reinforcement, the elastic length L_e and plastic length L_p along the bar are obtained as:

$$L_e = \frac{\min\left(\sigma, f_y\right) d_b}{4\tau_{be}} \tag{16}$$

$$L_p = \frac{\max\left(0, \sigma - f_y\right) d_b}{4\tau_{by}} \tag{17}$$

where σ is the reinforcement stress at the crack corresponding to strain ε, f_y is the yield strength of the steel, and d_b is the bar diameter. As shown in Fig. 7, lengths L_e and L_p allow to obtain the complete strain profile along the bar on either side of the crack. The two sides differ depending on the available anchorage length $L_{an,k}$. The anchorage can be provided by an anchor head or hook (left side), or can occur as an effective anchorage halfway to the neighbouring re-entrant corner crack (right side). Assuming a zero slip halfway through the re-entrant corner crack allows to study the shear crack in isolation from the corner (flexural) crack. The reinforcement pullout from one side s_k is obtained by integrating the strain diagram from the crack to the end of the anchorage length:

$$s_k = \frac{\min(\varepsilon,\varepsilon_y)L_e}{2} + \frac{(\varepsilon+\varepsilon_y)L_P}{2} - \max\left\{0.5\left[\frac{(\varepsilon-\varepsilon_y)\max(0,L_P-L_{an,k})}{L_P} + 2\varepsilon_y\right]\max(0,L_P-L_{an,k}),0\right\} + \frac{\min(\varepsilon,\varepsilon_y)\left\{\max\left[L_e+\min(0,L_P-L_{an,k}),0\right]\right\}^2}{2L_e} \tag{18}$$

Finally, the crack displacement for a given reinforcement strain in the crack is:

$$w_{bar} = s_{k=1} + s_{k=2} \tag{19}$$

However, within the framework of the kinematic model, the problem needs to be solved in a reversed manner. The model provides the crack displacement $w_{bar} = f(\varnothing, \Delta_{cc}, \Delta_{cs})$, and it is necessary to calculate the strain ε (and stress σ) corresponding to this displacement. Due to the form of Eqs. (16)-(19), this requires an iterative solution procedure such as Newton-Raphson or bisection methods. As a result, the forces in all horizontal, vertical and diagonal bars in the dapped-end region can be calculated for a given set of kinematic parameters $\varnothing$, Δ_{cc} and Δ_{cs}. The operations described in this section can be mathematically presented as a function f_{TCM}:

$$F_{bar} = f_{TCM}(\varnothing, \quad \Delta_{cc}, \Delta_{cs}) \tag{20}$$

Generally, Eq. (20) is applied to all horizontal, diagonal, and vertical bars (dapped-end stirrups) crossing the critical shear crack. However, vertical bars with bottom anchorage completely falling within the horizontal tension chord are neglected in the calculations. These are typically the vertical bars closest to the support plate and are not effective in carrying shear as the horizontal crack opening w_h is dominant and the vertical crack opening w_v is not sufficient to cause significant tension. As this effect is not reflected by the w_v profile of the assumed kinematics, such stirrups are conservatively neglected. The depth of the horizontal tension chord is estimated as $2(c + d_{bh}/2)$ from the bottom edge of the dapped end, where c and d_{bh} are concrete cover and horizontal bar diameter, respectively.

3.3. Aggregate interlock

The aggregate interlock shear V_{ci} is evaluated using the Contact Density Model (CDM) proposed by Li et al. [23]. This model uses the crack width w and slip s as inputs, and evaluates the shear stress and the normal stress on the crack. For simplicity, in this study the normal stresses are neglected, and the shear stresses are reduced by a factor of 0.18 as proposed elsewhere [19].

For a given set of kinematic parameters $\varnothing$, Δ_{cc} and Δ_{cs}, the crack widths w and crack slip s are evaluated at the midpoint of the shear crack from the compatibility conditions given by Eqs. (2)-(3). Then, this point is analysed using the CDM to evaluate the aggregate interlock shear stress v_{ci}. Subsequently, the total aggregate interlock force V_{ci} acting along the crack is obtained as:

$$V_{ci} = v_{ci} b l_{cr} \sin\alpha \tag{21}$$

where b and l_{cr} are width of the dapped end and length of the critical shear crack, respectively. This operation is mathematically presented as a function f_{ci}:

$$V_{ci} = f_{ci}(\varnothing, \Delta_{cc}, \Delta_{cs}) \tag{22}$$

3.4. Dowel action

Finally, the shear resisted by dowel action V_d of the main horizontal reinforcement is discussed (Fig. 5). This force is evaluated based on the DOF Δ_c, using a fixed-fixed beam type dowel model [19], with a limit imposed to account for the yielding of horizontal reinforcement:

$$V_d = \frac{n_b 12 E_s \pi d_b^4}{64 l_k^3}\Delta_c \le \frac{n_b f_y d_b^3}{3 l_k}\left[1 - \left(\frac{\sigma}{f_y}\right)^2\right] \tag{23}$$

where, n_b is the number of bars, d_b is the bar diameter, f_y is the yield strength of the bars, σ is the bar stress (see Section 3.2), and l_k is the length of bar-dowels. Length l_k is conservatively estimated as the distance between the inside edge of the support plate and the re-entrant corner of the dapped-end connection. It is assumed that the dowel length and the associated cover splitting is well controlled on the side where dowel is pushing against the concrete cover, due to the presence of the support plate. Eq. (23) can be mathematically presented as a function f_d:

$$V_d = f_d(\varnothing, \Delta_{cc}, \Delta_{cs}) \tag{24}$$

4. Equilibrium conditions and solution procedure

In Section 3, the relationships and procedures for calculating the shear-resisting forces for given DOFs $\varnothing$ and Δ_c were described. These relationships were generalized in Eqs. (12), (20), (22) and (24), and allow to obtain all the forces in the free-body diagrams in Fig. 5. To develop a global solution procedure, one of the two DOFs needs to be selected as a control parameter, and the other is obtained by solving equilibrium conditions. In this study, Δ_c is controlled from zero until the failure of the connection, while $\varnothing$ is calculated as described in the following.

The equilibrium conditions are written for the concrete block above the critical shear crack (Fig. 5):

- Moment equilibrium about point O (Fig. 5 left)

$$V = \frac{\begin{bmatrix} V_d x_h \cos\alpha + \sum F_{ha} x_{ha} \cos\alpha \\ + F_h x_h \sin\alpha \\ + F_v x_v \cos\alpha + F_d x_d \sin(\alpha+\beta) \end{bmatrix}}{\left(l_{cr}\cos\alpha + 0.5 l_{sp}\right)} \tag{25}$$

where x_h, x_{ha}, x_v, x_d are the lengths measured along the crack from point O to the various layers of reinforcement.

- Equilibrium of vertical forces (Fig. 5 right)

$$V = V_d + V_{ci} + V_{CLZ} + F_v + F_d \sin\beta \tag{26}$$

For a selected value of Δ_c and a guessed value of $\varnothing$, the unbalanced shear force from these two equations is:

$$V_{unb} = V_{Eq.\ (26)} - V_{Eq.\ (25)} \tag{27}$$

The solution procedure aims to bring V_{unb} to zero by varying $\varnothing$. The equilibrium conditions can be mathematically represented by the following function:

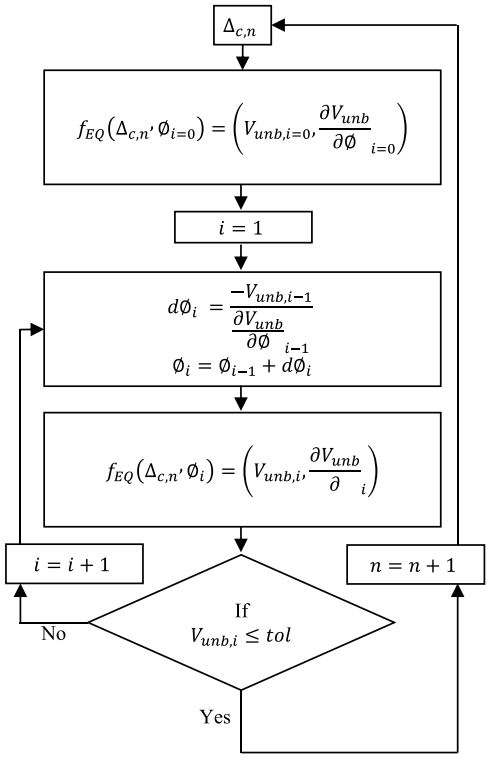

Fig. 8. Global Newton-Raphson solution procedure of kinematics-based model.

$$f_{EQ}(\Delta_c, \varnothing) = \left(V_{unb}, \frac{\partial V_{unb}}{\partial \varnothing}\right) \tag{28}$$

where $\frac{\partial V_{unb}}{\partial \varnothing}$ is the partial derivative of V_{unb} with respect to $\varnothing$. The Newton-Raphson method is used to iteratively bring V_{unb} to zero.

The known DOF at the start of the n^{th} load step is $\Delta_{c,n}$, and the first estimate for the unknown DOF $\varnothing_{i=0}$ is the value from the previous converged step $\varnothing_{n-1}$. With these values, function f_{Eq} is evaluated first.

$$f_{EQ}(\Delta_{c,n}, \varnothing_{i=0}) = \left(V_{unb,i=0}, \frac{\partial V_{unb}}{\partial \varnothing'}_{i=0}\right) \tag{29}$$

Based on the results, the next estimate for the unknown DOF $\varnothing_{i=1}$ can be calculated as follows:

$$d\varnothing_{i=1} = \frac{-V_{unb,i=0}}{\frac{\partial V_{unb}}{\partial \varnothing}_{i=0}} \tag{30}$$

$$\varnothing_{i=1} = \varnothing_{i=0} + d\varnothing_{i=1} \tag{31}$$

Using these updated values, the function f_{Eq} is evaluated again:

$$f_{EQ}(\Delta_{c,n}, \varnothing_{i=1}) = \left(V_{unb,i=1}, \frac{\partial V_{unb}}{\partial \varnothing'}_{i=1}\right) \tag{32}$$

This procedure is repeated until $V_{unb,i}$ converges to zero, and thus the corresponding value of $\varnothing_i$ satisfies the global equilibrium for the given $\Delta_{c,n}$. The global procedure is summarized with the flow chart in Fig. 8.

5. Failure modes

According to the proposed kinematics-based model, the failure of dapped-end connections can be triggered in three different ways along the critical shear crack:

1) Crushing of the concrete in the critical loading zone (CLZ) at the top of the crack;

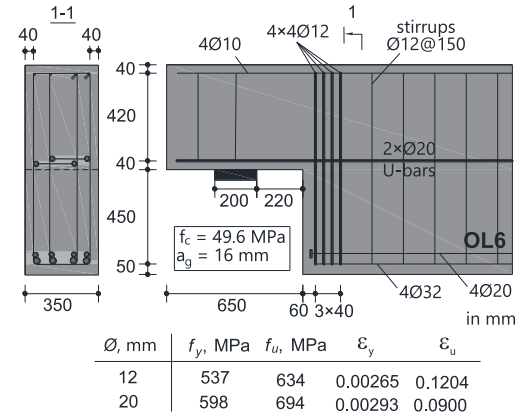

Ø, mm	f_y, MPa	f_u, MPa	ε_y	ε_u
12	537	634	0.00265	0.1204
20	598	694	0.00293	0.0900

(a) Geometry and reinforcement layout

(b) Photograph after failure

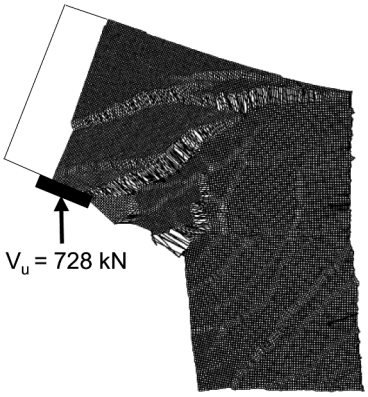

(c) Experimental deformed shape at peak load (x20)

Fig. 9. Details of specimen OL6 [17].

2) Yielding of the vertical hanger reinforcement in the critical shear crack prior to concrete crushing in the CLZ;
3) Yielding of all reinforcement in the shear crack other than some of the hanger bars.

The first two failure modes have been observed multiple times in experimental studies – see for example Fig. 2b. They often occur simultaneously as yielding of the hanger bars inflicts large damage in the concrete (compression softening), and subsequently leads to concrete crushing in the CLZ.

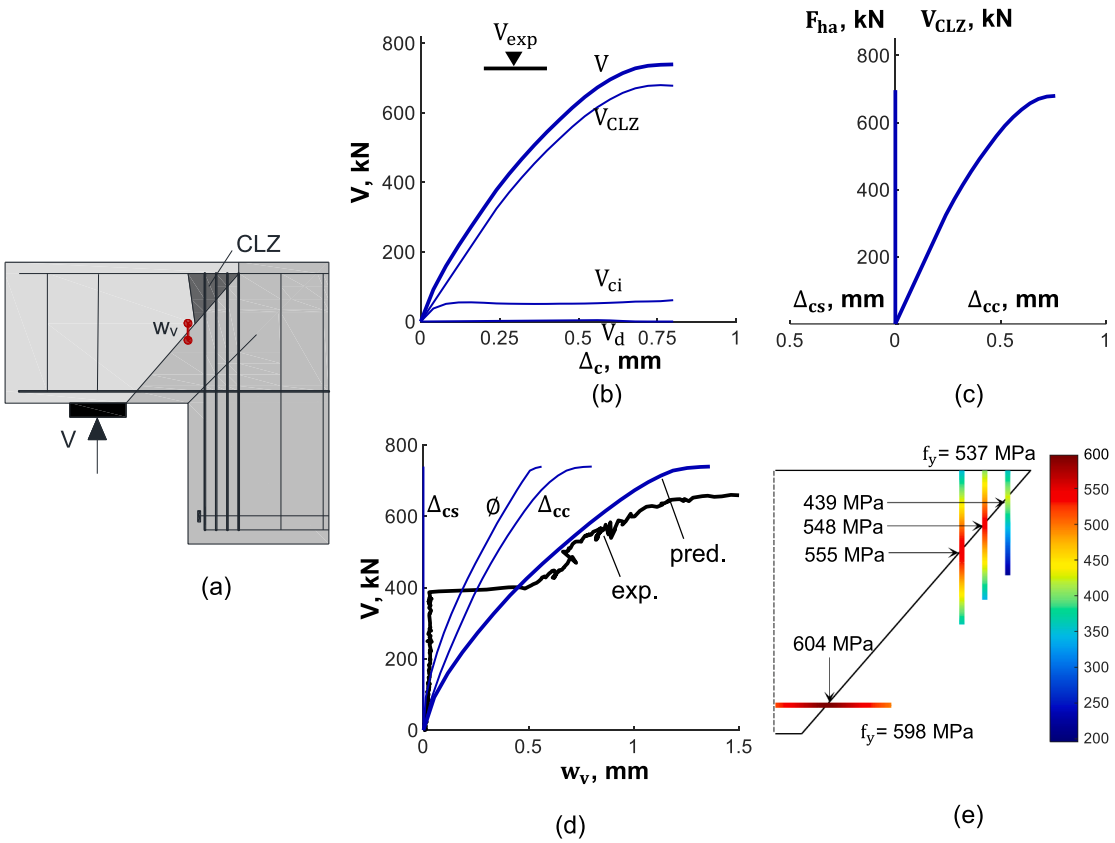

Fig. 10. Analysis results and measured response of dapped-end connection OL6 [17].

Kinematically, the third failure mode occurs with large plastic rotations in the critical crack about the CLZ. However, this failure mode is unlikely to occur in reality as it will be preceded by a flexural failure along the re-entrant corner crack. This is because the reinforcement stresses in the corner crack are typically higher than in the shear crack [5]. Therefore, the strength prediction obtained with the proposed shear model must be limited by the capacity obtained with an appropriate flexural model. Such a model has been proposed by Rajapakse et al. [10] on the basis of the kinematics of the re-entrant corner crack. Finally, it should be noted that the proposed kinematics-based model does not account for failures due to inadequate anchorage of the reinforcement.

6. Experimental validation

The proposed model is validated using lab experiments available in the literature. A set of 44 dapped ends are collected from the studies by Rajapakse et al., 2024 [18], Ferreira et al., 2023 [24], Rajapakse et al., 2022 [17], and Mata-Falcón, 2015 [5]. In this set, 24 specimens have orthogonal reinforcement and 20 specimens have diagonal reinforcement. The depth of the dapped ends are either 300 mm or 500 mm, and the total area of dapped-end reinforcement varies from 494 mm^2 to 4678 mm^2. The details of the specimens are provided in the Appendix A.

6.1. Detailed analysis of specimen OL6

The capabilities of the proposed model are first illustrated with the help of specimen OL6 with orthogonal reinforcement [17]. The geometry, reinforcement and material properties of this dapped end are shown in Fig. 9a. The failure mode was reported as shear failure with crushing of the concrete near the top end of the hanger bars. Fig. 9b shows a photograph of the specimen after failure and Fig. 9c shows the measured deformed shape at peak load.

The specimen was analysed using the proposed model by incrementally increasing Δ_c as described in Section 4. Fig. 10 provides a summary of important results from the analysis, which are compared to experimental data.

Fig. 10a shows the geometry of the kinematic model, including the shape and size of the CLZ (to scale) at the top of the hanger reinforcement. Fig. 10b shows the predicted shear force V versus Δ_c response, together with the predicted contributions of the different shear-carrying mechanisms. The specimen did not have stirrups in the dapped end, and therefore the contributions are only three: critical loading zone, aggregate interlock, and dowel action of the horizontal reinforcement. It can be seen that in this case the response is dominated by the CLZ, which accounts for 92 % of the predicted strength. The aggregate interlock accounts for 8 % while the contribution from the dowel action is zero due to the yielding of horizontal reinforcement at failure. The shear strength experimental-to-predicted ratio is 0.99 (728 kN/ 739 kN).

Fig. 10c provides more information on the predicted failure mode. It shows the responses of the CLZ and the hanger reinforcement. It can be seen that the CLZ crushes and enters the post-peak regime before the complete yielding of the hanger reinforcement. This result is consistent with the photograph in Fig. 9b, where concrete crushing and spalling is visible in the critical loading zone. According to the model, Δ_{cs} is zero throughout the analysis, and thus DOF Δ_c comes only from the deformation in the CLZ Δ_{cc}. This is consistent with the experimental deformed shape in Fig. 9c, where the vertical shift in the top branch of the critical crack nearly vanishes at the farthest hanger bar (stirrup).

Plots 10d shows how the shear crack opens with increasing load up to failure. As evident from the measured $V-w_v$ response, the shear crack formed at $V \approx 400kN$. The model assumes the critical shear crack is present throughout the analysis and therefore unable to predict the load level of crack formation. However, the opening of the critical shear crack is well predicted from the formation of the critical shear crack until failure. According to the model, rotation ∅ and displacement Δ_{cc} in the CLZ have approximately equal contribution to w_v, while Δ_{cs} is zero and

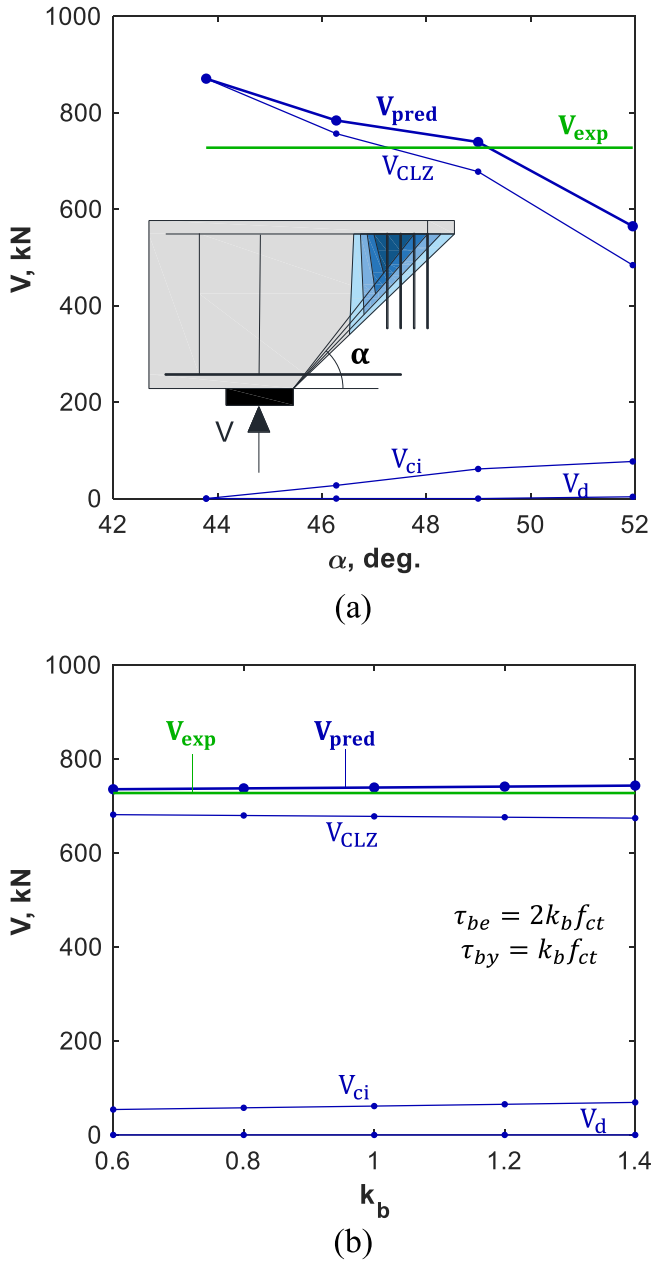

Fig. 11. Sensitivity of crack angle and bond strength on the shear strength of dapped-end connections.

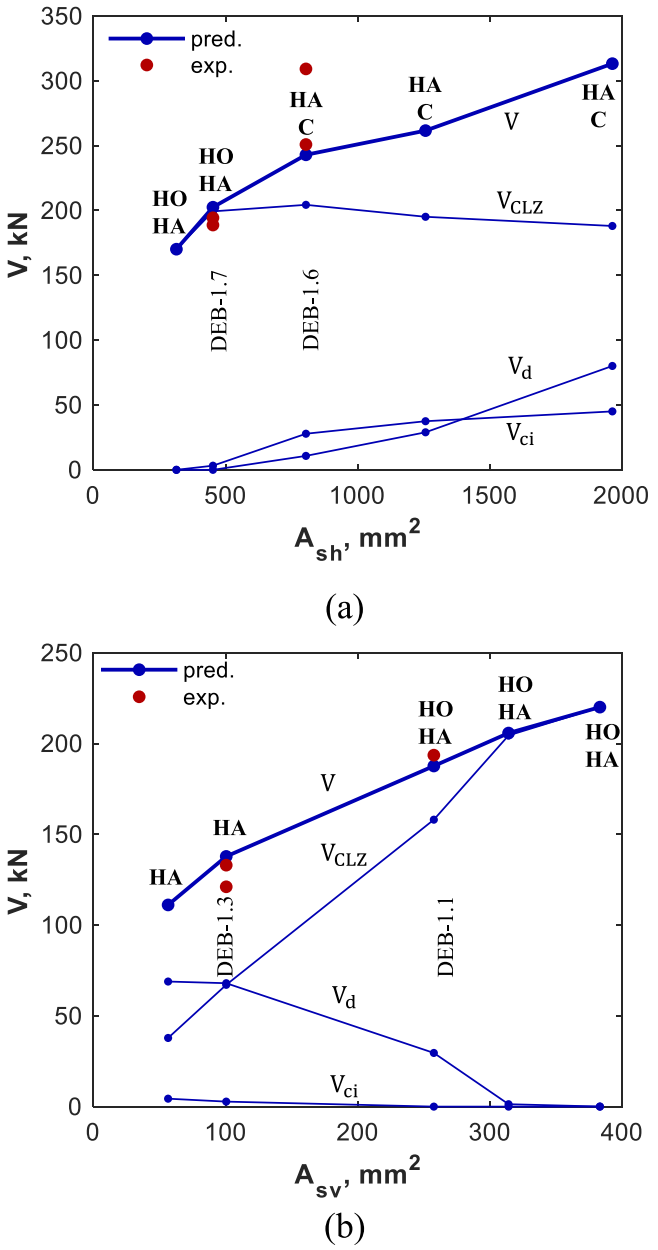

Fig. 12. Influence of (a) horizontal reinforcement and (b) hanger reinforcement on the strength and failure mode.

thus does not contribute to the crack.

Finally, the predicted reinforcement stresses at the peak load are shown in Fig. 10e. It can be seen that the horizontal bars and two out of the three hanger reinforcement bars yield at failure. In general, it can be observed that the predicted strength, failure mode, and shear crack widths are reasonably well captured by the model for this specimen.

6.2. Sensitivity analysis

To investigate the impact of model parameters on the predictions, a sensitivity analysis is performed on specimen OL6 [17]. The parameters investigated are crack angle α, compression softening factor k_c, and bond strengths τ_{be} and τ_{by}.

Fig. 11a shows variations of the strength of specimen OL6 [17] by changing the crack angle α in the model. The change in α is achieved by changing the top point of the assumed crack, keeping the bottom point fixed at the inside edge of the support plate. When the crack angle is increased, the size of the CLZ decreases along with its strength contribution V_{CLZ}, and the dapped-end strength. At the same time, increasing the crack angle increases the contribution of the aggregate interlock V_{ci} as the vertical component of aggregate interlock force increases. The predicted strength deviates approximately 20 % from the measured strength when the crack angle is varied. The proposed model assumes that the critical shear crack is propagated from the inside edge of the support plate to the top of the furthest hanger bar from the re-entrant corner. This assumption is consistent with assumptions made in strut-and-tie modelling of dapped-end connections, where the width of the nodal regions is determined based on the width of spread of the hanger reinforcement (see Section 6.4 and Appendix B for strut-and-tie modelling). The analysis was also repeated with and without accounting for compression softening in the CLZ ($k_c < 1$ as in Eq. (10) and $k_c = 1$, respectively). It was observed that the strength was increased by approximately 9 % when compression softening was neglected.

Fig. 11b shows the variation of predicted strength for specimen OL6

[17] with varying bond strengths. The change in bond was achieved by varying factor k_b from 0.6 to 1.4 in the expressions $\tau_{be} = 2k_b f_{ct}$ and $\tau_{by} = k_b f_{ct}$. The plot shows that for this dapped end the increase of bond strength causes a slight increase in the aggregate interlock contribution and the shear strength. When the bond strength is increased, DOF ∅ at peak load decreases due to the stiffer response of the horizontal reinforcement. However, DOF Δ_c remains unchanged as the response of the CLZ is not affected by bond. As a result, the aggregate interlock contribution increases while the contribution from the CLZ remains unchanged.

6.3. Effect of reinforcement amount and distribution on the shear strength

The strength of dapped-end connections is strongly influenced by the amount and distribution of the main horizontal and hanger reinforcement in the connection. This effect is studied in Fig. 12 with the help of tests DEB 1.7, DEB 1.6, DEB 1.3, and DEB 1.1 by Mata-Falcon [5]. The details of these specimens are provided in the Appendix A.

Fig. 12a shows measured and predicted shear strengths of dapped ends with a constant hanger reinforcement and increasing horizontal reinforcement. The five prediction points are obtained with various horizontal bars: 4Φ10, 4Φ12, 4Φ16, 4Φ20, and 4Φ25. The second and third predictions correspond to specimens DEB 1.7 and DEB 1.6, respectively. It can be seen that the model captures reasonably well the shear strength of the specimens. According to the model, when the horizontal reinforcement is increased 6.3 times from A_{sh} of 314 mm^2 to 1963 mm^2, the strength increases 1.8 times. The failure mode changes with increasing reinforcement: from yielding of all reinforcement (horizontal HO and hanger HA) to a combination of concrete crushing in the CLZ and yielding of the hangers (C and HA). In the range of CLZ crushing, the V_{CLZ} strength contribution is approximately constant. The aggregate interlock and dowel action contributions V_{ci} and V_d increase with increasing A_{sh}, but remain significantly smaller than the V_{CLZ}. Component V_{ci} increases because the width of the shear crack at failure decreases. Component V_d increases because the strains in the horizontal reinforcement at failure decrease.

In a similar format to Fig. 12a, Fig. 12b shows the influence of increasing hanger reinforcement on the strength of dapped ends with constant horizontal reinforcement. The five predictions points correspond to specimens with various hanger bars: 2Φ6, 2Φ8, 2Φ10 + 2Φ8, 4Φ10, and 2Φ10 + 2Φ12. The second and third predictions correspond to specimens DEB 1.3 and DEB 1.1, respectively, and they agree well with the measured strengths. The predictions show that when hanger reinforcement is increased 6.8 times from A_{sv} of 57 mm^2 to 384 mm^2, the strength increases 2 times. The failure mode changes with increasing hanger bars: from yielding of hanger bars (HA) to yielding of all the reinforcement (horizontal HO and hanger HA). In all the five predictions, the contribution from the CLZ is governed by the strength of the hanger bars, thus it increases with A_{sv}. With increasing hanger bars, the contribution from dowel action V_d reduces due to the increase of reinforcement strains in the horizontal bars at failure. The small contribution of the aggregate interlock V_{ci} reduces to zero due to the increase of the shear crack width at failure, with the increase of hanger reinforcement.

6.4. Strength and crack width predictions

The proposed model is also tested for all 44 specimens in the test database (Appendix A). This section first presents the strength predictions for all 44 tests and the shear crack width predictions for selected tests where the experimental measurements are available.

As mentioned in Section 5, the predicted capacity is obtained as the minimum of two values: the shear strength from the proposed model and the flexural strength from the model by Rajapakse et al. [10]. Out of the 44 specimens, the prediction of the proposed shear model governs in 13 cases. Fig. 13 shows the strength experimental-to-predicted ratios of the

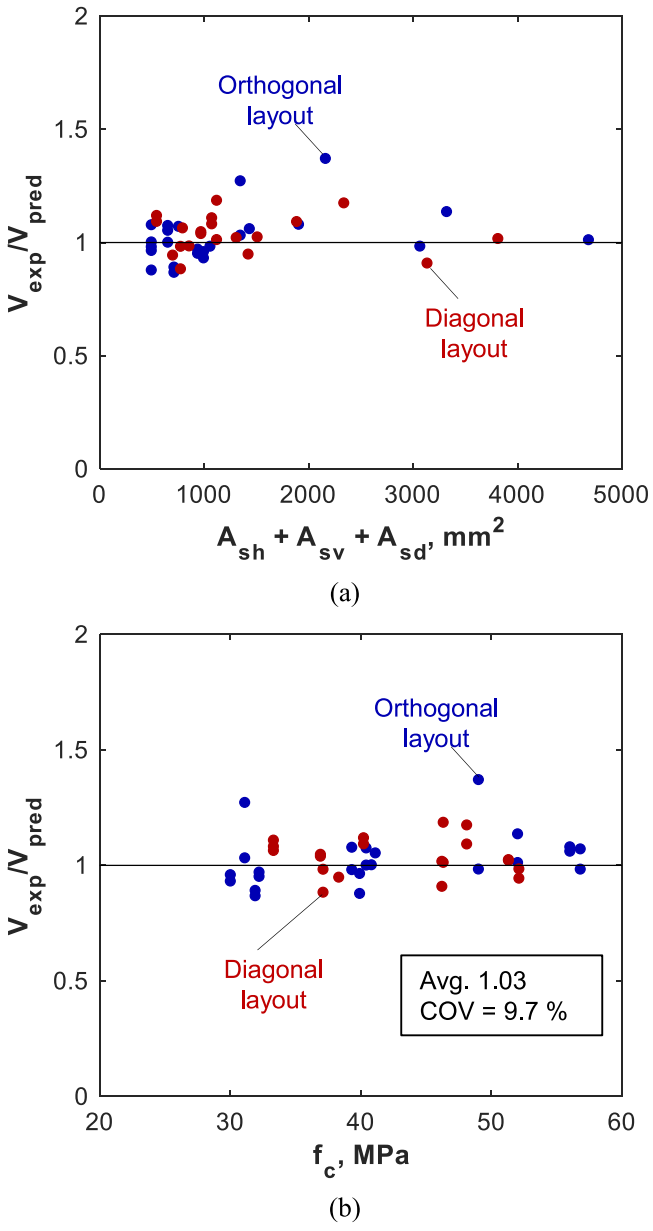

Fig. 13. Experimental-to-predicted strength ratios of 44 tests plotted as functions of test variables.

specimens, while the individual values are provided in the Appendix A. The ratios are plotted as a function of the total area of dapped-end reinforcement and the concrete compressive strength. It can be seen that the points are well grouped near the $V_{exp}/V_{pred} = 1$ line and do not show a clear bias with respect to the two test variables. The overall average ratio V_{exp}/V_{pred} was 1.03, with a coefficient of variation (COV) of 9.7 %. For the shear-critical specimens, the average ratio was 1.05 with a COV of 13.6 %, while for the flexure-critical specimens, the average ratio was 1.02 with a COV of 7.6 %. Considering the sensitivity study performed in Fig. 11a, some of the scatter in the predictions can be attributed to variations in the angle and location of the critical cracks in the tests.

To put these results into context, strength calculations were also performed with strut-and-tie models. The models and there parameters are described in Appendix B, while the resulting strength predictions V_{STM} are summarized in Appendix A. The strut-and-tie model is more conservative than the kinematics-based model and also exhibits higher scatter: an average V_{exp}/V_{STM} ratio of 1.27 and a COV of 23.2 %.

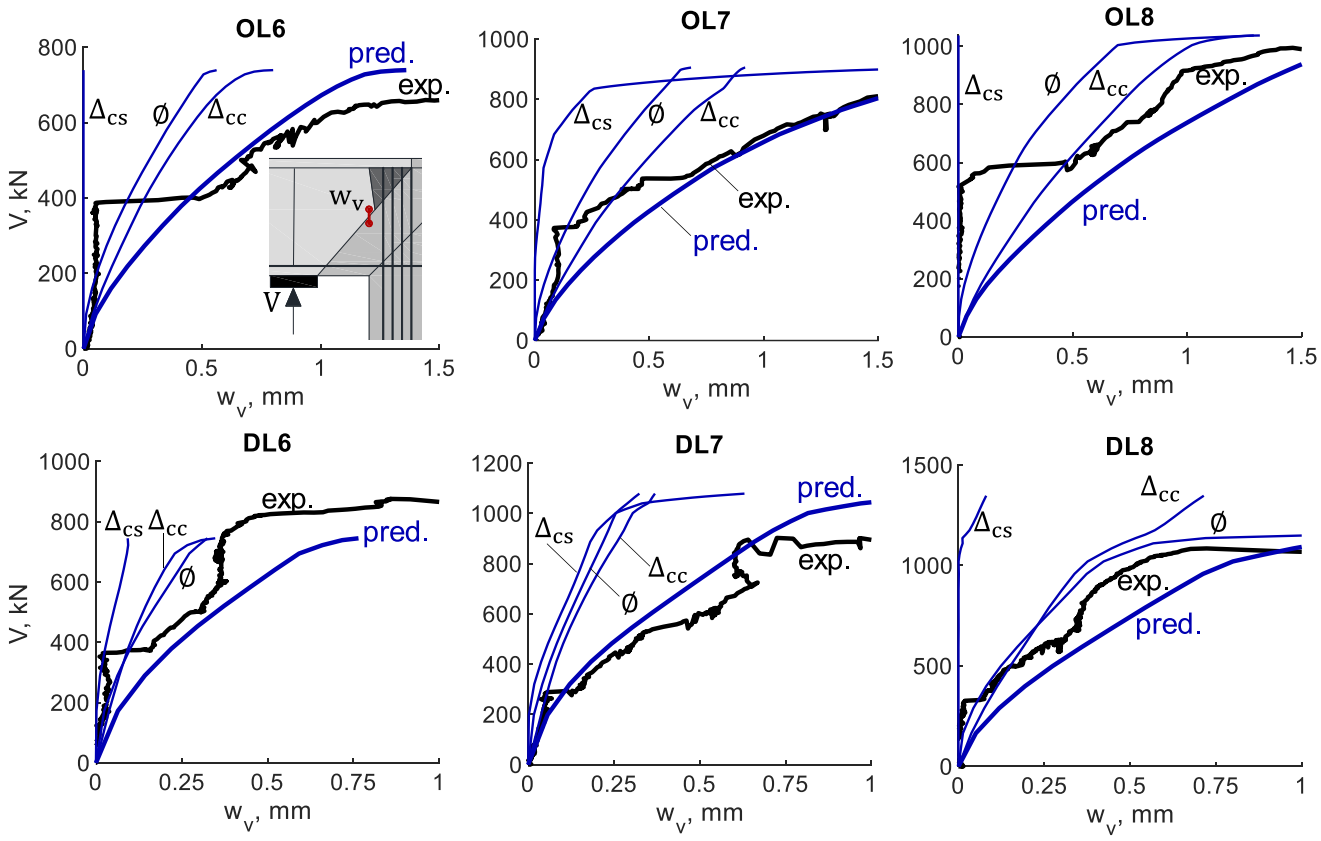

Fig. 14. Kinematics-based model predictions of shear crack widths of test specimens by Rajapakse et al. [17] [18].

Fig. 14 shows the measured and predicted vertical crack opening for six of the specimens tested by Rajapakse et al. [17] [18]. These specimens were the most shear-critical connections of the test program as they had the highest reinforcement intensity at the re-entrant corner. They include both orthogonal and diagonal reinforcement layouts. In addition to the shear crack opening, the plots also show the predicted contributions from the DOFs Δ_{cc}, Δ_{cs}, and $\varnothing$ to the opening. It can be observed that the model predicts the shear crack width reasonably well from the formation of the crack up to failure. It can also be seen that while DOF Δ_{cs} is zero for specimens OL6 and OL8, its contribution to the crack opening is significant in the rest of the studied dapped ends. In specimens OL7 and DL7, DOF Δ_{cs} increases rapidly prior to failure which shows yielding of all legs of hanger reinforcement.

7. Summary and conclusions

In this paper, a kinematics-based model was proposed for the shear behaviour of reinforced concrete dapped-end connections. The deformations of flexure- and shear-critical connections were studied using DIC measurements from a recent experimental program. On this basis, a kinematic model with two degrees of freedom (DOFs) was proposed, capable of describing the kinematics of the critical shear crack in the dapped end (widths and slips). The shear resisting mechanisms – reinforcement forces, concrete in compression, aggregate interlock, and dowel action – were evaluated for a given set of DOFs using the tension code model, Popovic's compression model, the contact density model, and a beam-type dowel model, respectively. The equilibrium of these forces allowed to iteratively calculate the applied load for a given controlling degree of freedom, and thus to predict the full response of the connection.

The proposed model was validated with 44 large-scale tests of dapped ends with a wide range of properties including both orthogonal and diagonal reinforcement layouts. The model produced an average experimental-to-predicted strength ratio of 1.03 and a coefficient of variation of 9.7 %. According to the model, shear failures can occur in different ways: yielding of all vertical, horizontal and hanger reinforcements, yielding of hanger reinforcement only, concrete crushing combined with hanger reinforcement yielding. It was shown that, as the model accounts for these failure modes, it captures the complex variation of shear strength with important dapped-end characteristics such as the amount and distribution of horizontal and hanger reinforcement. This can allow engineers to perform refined calculations and optimize the shear design of dapped-end connections.

CRediT authorship contribution statement

Sameera Hippola: Writing – original draft, Visualization, Validation, Software, Methodology, Investigation, Conceptualization. **Boyan I. Mihaylov:** Writing – review & editing, Supervision, Resources, Project administration, Methodology, Investigation, Conceptualization.

Declaration of Competing Interest

The authors declare that they have no known competing financial interests or personal relationships that could have appeared to influence the work reported in this paper.

Acknowledgements

This research was partially funded by the Joseph Deprez Foundation of University of Liège: Sameera Hippola, grant holder of Joseph Deprez Foundation.

Appendix A

No.	Ref.	ID	h (mm)	b (mm)	a (mm)	*Horizontal r/f*	f_{yh} (MPa)	spc_v (mm)	*Hanger r/f*	f_{yv} (MPa)	*Diagonal r/f*	f_{yd} (MPa)	l_{sp} (mm)	f_c (MPa)	a_g (mm)	V_{exp} (kN)	V_{flex} (kN)	V_{shear} (kN)	V_{pred} (kN)	$\frac{V_{exp}}{V_{pred}}$	$\frac{V_{exp}}{V_{STM}}$
1	[24]	REF−01	325	250	235	3Φ12	530	100	3 × 2Φ10	527	2Φ14	507	100	46.3	15	359	302	353	302	1.19	1.39
2		REF−02	325	250	235	3Φ12	530	100	3 × 2Φ10	527	2Φ14	507	100	46.3	15	306	302	353	302	1.01	1.19
3	[18]	DL1	500	350	380	2Φ12	537	-	2Φ10	509	1Φ20	598	200	52.1	16	259	274	293	274	0.94	1.12
4		DL2	500	350	380	2Φ12	537	60	2 × 2Φ10	509	1Φ20	598	200	52.1	16	299	303	316	303	0.98	1.22
5		DL3	500	350	380	2Φ16	599	60	4Φ8 + 2Φ8	521	3Φ16	599	200	51.3	16	520	509	537	509	1.02	1.10
6		DL4	500	350	380	2Φ16	599	60	2 × 4Φ8 + 2Φ8	521	3Φ16	599	200	51.3	16	555	541	599	541	1.02	1.14
7		DL5	500	350	380	2Φ20	598	-	4Φ12	537	4Φ16	599	200	48.1	16	782	716	776	716	1.09	1.31
8		DL6	500	350	380	2Φ20	598	60	2 × 4Φ12	537	4Φ16	599	200	48.1	16	876	797	745	745	1.18	1.39
9		DL7	500	350	380	2Φ25	540	80	4Φ12 + 2Φ12	537	3Φ25	540	200	46.2	16	905	995	1079	995	0.91	0.87
10		DL8	500	350	380	2Φ25	540	80	3 × 4Φ12	537	3Φ25	540	200	46.2	16	1085	1066	1347	1066	1.02	1.12
11	[17]	OL1	500	350	380	4Φ12	537	60	4Φ8 + 2Φ8	521	-	-	200	56.8	16	245	229	257	229	1.07	1.56
12		OL2	500	350	380	4Φ12	537	60	3 × 4Φ8	521	-	-	200	56.8	16	283	290	288	288	0.98	1.27
13		OL3	500	350	380	4Φ16	599	60	2 × 4Φ10	509	-	-	200	56	16	472	444	452	444	1.06	1.47
14		OL4	500	350	380	4Φ16	599	60	3 × 4Φ10 + 2Φ10	509	-	-	200	56	16	555	514	557	514	1.08	1.32
15		OL5	500	350	380	4Φ20	598	60	2 × 4Φ12	537	-	-	200	49	16	628	626	458	458	1.37	1.29
16		OL6	500	350	380	4Φ20	598	40	4 × 4Φ12	537	-	-	200	49	16	728	794	739	739	0.98	1.07
17		OL7	500	350	380	4Φ25	540	90	3 × 4Φ12	537	-	-	200	52	16	868	763	905	763	1.14	1.19
18		OL8	500	350	380	4Φ25	540	40	6 × 4Φ12	537	-	-	200	52	16	995	982	1037	982	1.01	1.13
19	[5]	DEB−1.1(T1)	300	250	240	5Φ10	566	-	(2Φ10 +2Φ8)	587	-	-	150	41.1	20	194	184	188	184	1.05	1.28
20		DEB−1.2(T1)	300	250	240	3Φ10	566	-	(2Φ10 +2Φ8)	587	-	-	150	39.3	20	146	143	135	135	1.08	1.19
21		DEB−1.2(T2)	300	250	240	3Φ10	566	-	(2Φ10 +2Φ8)	587	-	-	150	39.3	20	133	143	135	135	0.98	1.08
22		DEB−1.3(T1)	300	250	240	5Φ10	566	-	2Φ8	619	-	-	150	39.9	20	121	141	138	138	0.88	1.95
23		DEB−1.3(T2)	300	250	240	5Φ10	566	-	2Φ8	619	-	-	150	39.9	20	133	141	138	138	0.96	2.14
24		DEB−1.4(T1)	300	250	240	5Φ10	566	40	2Φ8 + 2Φ6 + 2Φ8	614	-	-	150	40.4	20	183	170	177	170	1.08	1.15
25		DEB−1.4(T2)	300	250	240	5Φ10	566	40	2Φ8 + 2Φ6 + 2Φ8	614	-	-	150	40.4	20	170	170	177	170	1.00	1.07
26		DEB−1.5(T1)	300	250	240	3Φ10	566	40	2Φ8 + 2Φ6 + 2Φ8	614	-	-	150	40.8	20	125	131	125	125	1.00	1.19
27		DEB−1.6(T1)	300	250	240	4Φ16	549	40	2Φ10 + 2Φ12 + 2Φ10	545	-	-	150	31.1	20	309	246	243	243	1.27	1.13
28		DEB−1.6(T2)	300	250	240	4Φ16	549	40	2Φ10 + 2Φ12 + 2Φ10	545	-	-	150	31.1	20	251	246	243	243	1.03	0.92
29		DEB−1.7(T1)	300	250	240	4Φ12	546	40	2Φ10 + 2Φ12 + 2Φ10	545	-	-	150	30	20	194	209	203	203	0.96	1.00
30		DEB−1.7(T2)	300	250	240	4Φ12	546	40	2Φ10 + 2Φ12 + 2Φ10	545	-	-	150	30	20	189	209	203	203	0.93	0.97
31		DEB−1.8(T1)	300	250	240	5Φ12	546	40	2Φ10 + 2Φ6 + 2Φ10	545	-	-	150	32.2	20	195	205	218	205	0.95	0.97
32		DEB−1.8(T2)	300	250	240	5Φ12	546	40	2Φ10 + 2Φ6 + 2Φ10	545	-	-	150	32.2	20	199	205	218	205	0.97	0.99
33		DEB−1.9(T1)	300	250	240	3Φ12	546	40	2Φ10 + 2Φ6 + 2Φ10	545	-	-	150	31.9	20	142	163	168	163	0.87	0.97
34		DEB−1.9(T2)	300	250	240	3Φ12	546	40	2Φ10 + 2Φ6 + 2Φ10	545	-	-	150	31.9	20	146	163	168	163	0.89	1.00
35		DEB−2.1(T1)	300	250	240	3Φ10	566	-	3Φ8	619	2Φ10	566	150	40.2	20	195	178	182	178	1.09	1.76
36		DEB−2.1(T2)	300	250	240	3Φ10	566	-	3Φ8	619	2Φ10	566	150	40.2	20	200	178	182	178	1.12	1.81
37		DEB−2.2(T1)	300	250	240	4Φ12	546	-	4Φ10	544	2Φ12 + 1Φ10	545	150	33.3	20	322	297	323	297	1.08	1.56
38		DEB−2.2(T2)	300	250	240	4Φ12	546	-	4Φ10	544	2Φ12 + 1Φ10	545	150	33.3	20	330	297	323	297	1.11	1.60
39		DEB−2.3(T1)	300	250	240	3Φ12	546	-	2Φ12	546	2Φ12	546	150	33.3	20	241	226	245	226	1.06	1.57
40		DEB−2.4(T1)	300	250	240	4Φ10	544	-	2Φ12	546	2Φ12 + 1Φ16	547	150	36.9	20	312	298	331	298	1.05	1.07
41		DEB−2.4(T2)	300	250	240	4Φ10	544	-	2Φ12	546	2Φ12 + 1Φ16	548	150	36.9	20	309	298	331	298	1.04	1.06
42		DEB−2.5(T1)	300	250	240	2Φ8 + 2Φ6	537	-	2Φ8	532	2Φ16 + 1Φ12	549	150	37.1	20	265	300	325	300	0.88	1.55
43		DEB−2.5(T2)	300	250	240	2Φ8 + 2Φ6	537	-	2Φ8	532	2Φ16 + 1Φ12	549	150	37.1	20	295	300	325	300	0.98	1.72
44		DEB−2.6(T1)	300	250	240	4Φ16	549	-	2Φ8	532	2Φ16 + 1Φ12	549	150	38.3	20	328	346	370	346	0.95	0.93
															Average					1.03	1.27
															COV (%)					9.7	23.2

h=height of dapped end, b=width of dapped end, a=distance from the support shear force to the first vertical reinforcement layer of the full-depth section, a'=distance from beam end to the outside edge of the support plate, f_{yh} = yield strength of horizontal reinforcement, spc_v=spacing between hanger reinforcement layers of the full-depth section, f_{yv} = yield strength of hanger reinforcement, f_{yd} = yield strength of diagonal reinforcement, l_{sp}=length of the support plate, f_c=concrete compressive strength, a_g=maximum aggregate size, V_{exp}=measured strength, V_{flex}=predicted flexural strength, V_{shear}=predicted shear strength, V_{pred}=min(V_{flex}, V_{shear}), V_{STM}=predicted strength from strut-and-tie modelling.

Appendix B

Details of the strut-and-tie modelling of specimens OL8 [17] and DL8 [18] are presented here. The stress limit for struts is $\sigma_{R,max} = 0.6\nu' f_c$ while the stress limit for nodes is $\sigma_{R,max} = 0.85\nu' f_c$, where $\nu' = 1 - f_c/250$ as recommended in EN 1992-1–1 (2004). Verified sections of the nodes are shown in green. The node geometries are given for the diagonal reinforcement layout. In the case of orthogonal layout, node A shape remains the same while node B will become a right-angled triangle with $C_2 = C_1$, $C_3 = 0$, $\theta_2 = \theta_1$, and $l_{n2,c2} = l_{n2}$. In the case of diagonal reinforcement layout, $l_{n2,c2} = l_{n2}C_2\sin\theta_2/(C_2\sin\theta_2 + C_3\sin\theta_3)$.

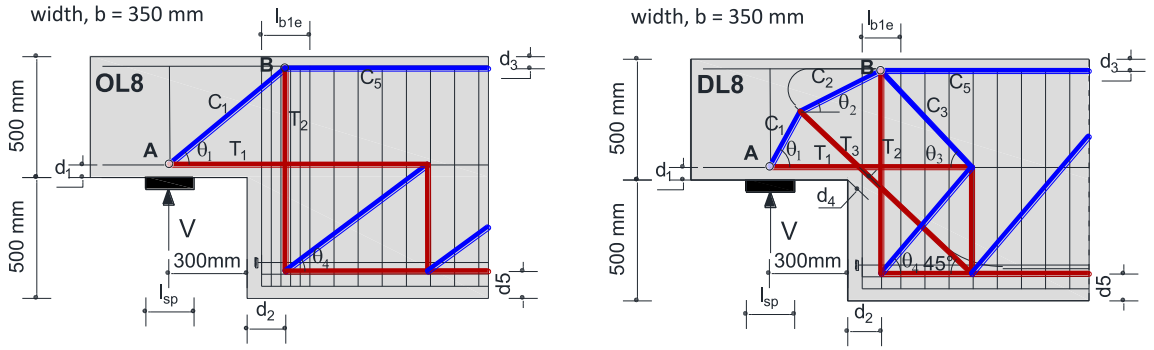

spec.	f_c,MPa	A_{sh},mm^2	f_{yh},MPa	A_{sv},mm^2	f_{yv},MPa	A_{sd},mm^2	f_{yd},MPa
OL8	52	1964	540	2712	537	-	-
DL8	46.2	982	540	1356	537	1473	540

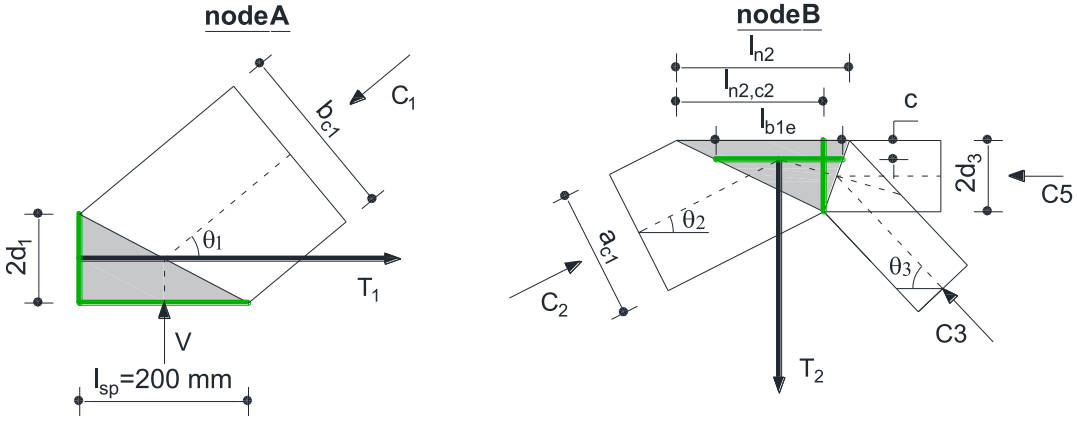

Fig B.1. Strut-and-tie model for specimens OL8 and DL8

Table B.1
Geometrical details of the strut-and-tie models for specimens OL8 and DL8

Spec.	l_{b1e} (mm)	d_1(mm)	d_2(mm)	d_3(mm)	d_4(mm)	d_5(mm)	θ_1(deg)	θ_2(deg)	θ_3(deg)	θ_4(deg)	b_{c1}(mm)	$l_{n2,c2}$(mm)	a_{c1}(mm)
OL8	200	52.5	160	50	-	111	39.6	-	-	39.6	208	333	289
DL8	160	52.5	140	50	73	111	61.2	25.7	48.4	51.4	226	227	189

Table B.2
Main calculation results for specimens OL8 and DL8

Specimen		$T_{1,u}$(kN)	T_{2u}(kN)	T_{3u}(kN)	$C_{u,top}$(kN)	$C_{u,bot}$(kN)	$n_{Au,T1}$(kN)	$n_{Au,V}$(kN)	$n_{Bu,c}$(kN)	$n_{Bu,T2}$(kN)	V_u(kN)
OL8	Strut/tie capacity	1061	1456	-	2493	1794	1283	2444	1586	2444	**878**
	Corresponding V	**878**	1456	-	1589	1144	1061	2444	1011	2444	
DL8	Strut/tie capacity	530	728	795	1491	1787	1176	2240	1243	2688	**964**
	Corresponding V	**964**	1231	1132	1284	1566	2139	2240	1070	4546	

T_{1u}=capacity of the horizontal tie T_1, T_{2u}=capacity of the vertical tie T_2, T_{3u}=capacity of the diagonal tie T_3 ,$C_{u,top}$=capacity of the strut C_1 or C_2 considering crushing at top, $C_{u,bot}$=capacity of the strut C_1 considering crushing at the bottom, $n_{Au,T1}$= capacity of the horizontal tie T_1considering the failure of vertical section of node A, $n_{Au,V}$= dapped-end strength considering the failure of horizontal section of node A, $n_{Bu,c}$= capacity of strut C_1 or C_2 considering the failure of vertical section of node B, $n_{2u,T2}$= capacity of the vertical tie T_2 considering the failure of horizontal section of node B.

Data availability

Data will be made available on request.

References

[1] Schlaich J, Schafer K, Jennewein M. Toward a consistent design of structural concrete. PCI J 1987;32(3):74–150.
[2] Schlaich J, Schafer K. Design and detailing of structural concrete using strut-and-tie models. Struct Eng 1991;69(6):113–25.
[3] Cook WD, Mitchell D. Studies of disturbed regions near discontinuities in reinforced concrete members. Struct J 1988;85(2):206–16.
[4] Mata-Falcón J, Pallares L, Miguel PF. Proposal and experimental validation of simplified strut-and-tie models on dapped-end beams. Eng Struct 2019;183:594–609.
[5] Mata-Falcón J. Serviceability and Ultimate Behaviour of Dapped-end Beams (In Spanish: Estudio del comportamiento en servicio y rotura de los apoyos a media madera). PhD Thesis. Universitat Politècnica de València; 2015.
[6] Muttoni A, Fernandez Ruiz M, Niketic F, Backes MR. Assessment of existing structures based on elastic-plastic stress fields - Modelling of critical details and investigation of the in-plane shear transverse bending interaction (Switzerland) Rapp OFROU 2016;N◦680 (Switzerland).
[7] Precast/Prestressed Concrete Institute. PCI design handbook (2010), 7th ed. Chicago (Illinois, USA); p. 828.
[8] Santarsiero G, Masi A, Picciano V. Durability of Gerber Saddles in RC bridges: analyses and applications (Musmeci Bridge, Italy). Infrastructures 2021;6(2):25.
[9] Nagy-Gyorgy T, Sas G, Daescu AC, Barros JA, Stoian V. Experimental and numerical assessment of the effectiveness of FRP-based strengthening configurations for dapped-end RC beams. Eng Struct 2012;44:291–303.
[10] Rajapakse C, Degée H, Mihaylov B. Assessment of failure along re-entrant corner cracks in existing RC dapped-end connections. Struct Eng Int 2021;31(2):216–26.
[11] Rajapakse Chathura. Behaviour and Modelling of Reinforced Concrete Dapped-End Connections. PhD Thesis. University of Liege and Hasselt University; 2023.
[12] CEN European Committee for Standardization. Eurocode 2. Design of concrete structures Part 1-1: General rules and rules for buildings. Brussels (Belgium): EN 1992-1-1; 2004.
[13] Building Code Requirements for Structural Concrete. American Concrete Institute: ACI 318-19; 2019.
[14] Vecchio FJ, Collins MP. The modified compression field theory for reinforced concrete elements subjected to shear. Acids Struct J 1986;83:219–31.
[15] Vecchio FJ. Disturbed stress field model for reinforced concrete: implementation. J Struct Eng 2001:12.
[16] Mihaylov BI, Bentz EC, Collins MP. Two parameter kinematic theory for shear behaviour of deep beams. Acids Struct J 2013;110(3):447–56.
[17] Rajapakse C, Degée H, Mihaylov B. Investigation of shear and flexural failures of dapped-end connections with orthogonal reinforcement. Eng Struct 2022;260:114233.
[18] Rajapakse C, Degée H, Mihaylov B. Investigation of shear and flexural failures of dapped-end connections with diagonal reinforcement. Acids Struct J 2024;121(4):35–46.
[19] Mihaylov BI. Five-spring model for complete shear behaviour of deep beams. Struct Concr 2015. No. 1.
[20] Popovics SA. Numerical approach to the complete stress-strain curve of concrete. Cem Concr Res 1973;3(5):583–99.
[21] Mihaylov BI, Hunt B, Bentz EC, Collins MP. Three-parameter kinematic theory for shear behavior of continuous deep beams. Acids Struct J 2015;112(1):47–58.
[22] Marti P, Alvarez M, Kaufmann W, Sigrists V. Tension chord model for structural concrete. Struct Eng Int 1998;8(4):287–98.
[23] Li B, Maekawa K, Okamura H. Contact Density Model for Stress Transfer Across Cracks in Concrete. J Fac Eng Univ Tokyo (B) 1989;40(1):9–52.
[24] Ferreira KF, Rampini MC, Zani G, Colombo M, Di Prisco M. Experimental investigation on the use of Fabric-Reinforced Cementitious Mortars for the retrofitting of reinforced concrete dapped-end beams. Struct Concr 2023:1–29.